Finite element resistivity modeling for three-dimensional structures with arbitrary anisotropy using secondary potentials

Yuguo Li and Klaus Spitzer
Institut für Geophysik, TU Bergakademie Freiberg

1 INTRODUCTION

The electrical inhomogeneity and anisotropy can produce strong orientational effects in resistivity measurements and soundings curves (Matias, 2002). To overcome this problem, several azimuthal electrode arrays are proposed, such as square arrays (Habberjam 1979), azimuthal Wenner and Schlumberger arrays (Leonard-Mayer 1984; Taylor & Fleming 1988) as well as azimuthal offset Wenner array (Watson & Barker 1999). Several successful applications have been reported in the literature (Busby 2000). However, numerical simulations for geoelectrical fields in anisotropic structures have rarely been discussed in the literature, especially for multidimensional anisotropic structures. The electrical potential due to a point source in a homogeneous anisotropic medium can be obtained by transforming Laplace's equation for a homogeneous isotropic medium into Laplace's equation for a homogeneous anisotropic medium by stretching and rotating a coordinate system (Bhattacharya & Patra 1968, Habberjam 1979). The effects of anisotropy for a layered structure was studied by Wait (1990), Li & Uren (1998) and Yin & Weidelt (1999). Verner & Pek (1998) presented a 2D finite difference algorithm for numerical modeling of direct currents in anisotropic structures.
In this paper, 3D anisotropic structures are studied using the finite element (FE) technique. In the following section, we describe the numerical realization of the FE algorithm in detail. We then verify the finite element algorithm using an anisotropic two-layered earth. Finally, we calculate the apparent resistivity of three types of anisotropy: horizontal, vertical and dipping anisotropy.

2 GOVERNING EQUATIONS AND BOUNDARY CONDITIONS

Consider a three-dimensional (3D) conductivity model with arbitrary anisotropy in a Cartesian system of coordinates (x,y,z) with z-axis pointing downwards. The current source I is located at a point (x_q,y_q,z_q). The corresponding source function is

$$q(x,y,z) = I\delta(x-x_q)\delta(y-y_q)\delta(z-z_q) \tag{1}$$

where δ is the Dirac delta function. The flow of the steady electric current obeys the equation of continuity

$$\nabla\cdot\mathbf{j}(x,y,z) = q(x,y,z), \tag{2}$$

where $\mathbf{j}$ denotes the current density. In the anisotropic earth, the current density $\mathbf{j}$ and the electric field $\mathbf{E}$ are in general no longer parallel, which is expressed by the generalized Ohm's law:

$$\mathbf{j} = \underline{\underline{\sigma}}\mathbf{E} = \underline{\underline{\rho}}^{-1}\mathbf{E}, \tag{3}$$

where

$$\underline{\underline{\sigma}} = \underline{\underline{\rho}}^{-1}, \qquad \underline{\underline{\rho}} = \begin{pmatrix} \rho_{xx} & \rho_{xy} & \rho_{xz} \\ \rho_{yx} & \rho_{yy} & \rho_{yz} \\ \rho_{zx} & \rho_{zy} & \rho_{zz} \end{pmatrix}$$

are the conductivity and the resistivity tensor, respectively. In the earth, these tensors are symmetric and positive definite, and when rotated into the directions of their principal axes (x',y',z'), they are given by

$$\underline{\underline{\sigma}}' = \begin{pmatrix} \sigma_{x'} & 0 & 0 \\ 0 & \sigma_{y'} & 0 \\ 0 & 0 & \sigma_{z'} \end{pmatrix}, \qquad \underline{\underline{\rho}}' = \begin{pmatrix} \rho_{x'} & 0 & 0 \\ 0 & \rho_{y'} & 0 \\ 0 & 0 & \rho_{z'} \end{pmatrix},$$

where $\sigma_{x'},\sigma_{y'},\sigma_{z'}$ are referred to as the principal conductivities, and $\rho_{x'},\rho_{y'},\rho_{z'}$ as the principal resistivities.

The stationary electric field $\mathbf{E}$ can be written as the negative gradient of the electric potential v:

$$\mathbf{E} = -\nabla v. \tag{4}$$

Substituting eqs. (1), (3) and (4) into equation (2), we have the following relation

$$\nabla \cdot (\underline{\underline{\rho}}^{-1}(x,y,z)\nabla v(x,y,z)) = -I\delta(x-x_q)\delta(y-y_q)\delta(z-z_q), \tag{5}$$

which is the differential equation of the electric potential $v(x,y,z)$ for a 3D conductivity distribution with arbitrary anisotropy.

Numerical approximations using equation (5) typically give poor results in the vicinity of the source location because of steep gradients around the source. In order to remove the effect of the singular potential caused by the source, the singularity removal procedure (Lowry et al. 1989; Zhao & Yedlin 1996) is applied. The potential v is then subdivided into a primary potential v_p and a secondary potential v_s:

$$v(x,y,z) = v_p(x,y,z) + v_s(x,y,z). \tag{6}$$

The primary potential v_p can be described by an analytical solution of the partial differential equation

$$\nabla \cdot (\underline{\underline{\rho_p}}^{-1}(x,y,z)\nabla v_p(x,y,z)) = -I\delta(x-x_q)\delta(y-y_q)\delta(z-z_q) \tag{7}$$

for a homogeneous anisotropic half-space with the resistivity tensor

$$\underline{\underline{\rho_p}} = \begin{pmatrix} \rho^p_{xx} & \rho^p_{xy} & \rho^p_{xz} \\ \rho^p_{xy} & \rho^p_{yy} & \rho^p_{yz} \\ \rho^p_{xz} & \rho^p_{yz} & \rho^p_{zz} \end{pmatrix},$$

if the current source is located on the ground surface ($z_q = 0$), yielding solution

$$v_p = \frac{I(\rho^p_{x'}\rho^p_{y'}\rho^p_{z'})^{1/2}}{2\pi}\frac{1}{B_p{}^{1/2}} \tag{8}$$

with

$$B_p = \rho^p_{xx}(x-x_q)^2 + 2\rho^p_{xy}(x-x_q)(y-y_q) + 2\rho^p_{xz}(x-x_q)z + \rho^p_{yy}(y-y_q)^2 + 2\rho^p_{yz}(y-y_q)z + \rho^p_{zz}z^2.$$

Here $\rho^p_{x'}, \rho^p_{y'}$ and $\rho^p_{z'}$ are the principal resistivities of the homogeneous anisotropic half-space.

Inserting eqs. (6) and (7) into (5), gives the differential equation for v_s:

$$\nabla \cdot (\underline{\underline{\rho}}^{-1}(x,y,z)\nabla v_s(x,y,z)) + \nabla \cdot (\underline{\underline{\rho_s}}^{-1}(x,y,z)\nabla v_p(x,y,z)) = 0, \tag{9}$$

with

$$\underline{\underline{\rho}}^{-1}(x,y,z) = \underline{\underline{\rho_s}}^{-1}(x,y,z) + \underline{\underline{\rho_p}}^{-1}. \tag{10}$$

Since no current crosses the ground surface denoted by Γ_s, the boundary conditions on Γ_s are given by

$$\frac{\partial v_p}{\partial n} = 0, \qquad \frac{\partial v_s}{\partial n} = 0 \qquad \text{on} \quad \Gamma_s, \tag{11}$$

where n is the outward normal direction of the ground surface Γ_s.
On the other domain boundaries denoted by Γ_∞, a mixed boundary condition is proposed. The total potential at large distances from sources and inhomogeneities has the general form of

$$v \approx \frac{I(\rho_{x'}\rho_{y'}\rho_{z'})^{1/2}}{2\pi}\frac{1}{B^{1/2}} \tag{12}$$

with

$$B = \rho_{xx}(x-x_q)^2 + 2\rho_{xy}(x-x_q)(y-y_q) + 2\rho_{xz}(x-x_q)z + \rho_{yy}(y-y_q)^2 + 2\rho_{yz}(y-y_q)z + \rho_{zz}z^2,$$

where $\rho_{x'}, \rho_{y'}$ and $\rho_{z'}$ are the principal resistivities of the anisotropic medium at model boundaries. Hence,

$$\underline{\underline{\rho}}^{-1}\frac{\partial v}{\partial n} = \underline{\underline{\sigma}}\nabla v \cdot \mathbf{n}$$

$$= -\frac{I(\rho_{x'}\rho_{y'}\rho_{z'})^{1/2}}{2\pi B^{3/2}} \begin{pmatrix} \sigma_{xx} & \sigma_{xy} & \sigma_{xz} \\ \sigma_{xy} & \sigma_{yy} & \sigma_{yz} \\ \sigma_{xz} & \sigma_{yz} & \sigma_{zz} \end{pmatrix} \begin{pmatrix} \rho_{xx}(x-x_q)+\rho_{xy}(y-y_q)+\rho_{xz}z \\ \rho_{xy}(x-x_q)+\rho_{yy}(y-y_q)+\rho_{yz}z \\ \rho_{xz}(x-x_q)+\rho_{yz}(y-y_q)+\rho_{zz}z \end{pmatrix} \cdot \mathbf{n},$$

where $\mathbf{n}$ is the outward normal direction of the boundary Γ_∞. After straightforward but tedious derivations, we get

$$\underline{\underline{\rho}}^{-1}\frac{\partial v}{\partial n} = -\frac{I(\rho_{x'}\rho_{y'}\rho_{z'})^{1/2}}{2\pi B^{3/2}}\mathbf{r}\cdot\mathbf{n} = -\frac{r\cos(r,n)}{B}v,$$

or

$$\underline{\underline{\rho}}^{-1}\frac{\partial v}{\partial n} + \frac{r\cos(r,n)}{B}v = 0, \tag{13}$$

where $r = |\mathbf{r}| = ((x-x_q)^2+(y-y_q)^2+z^2)^{1/2}$ denotes the radial distance from the source location to the boundary.

In a similar way, we can get the following relation

$$\underline{\underline{\rho_p}}^{-1}\frac{\partial v_p}{\partial n} + \frac{r\cos(r,n)}{B_p}v_p = 0 \tag{14}$$

for the primary potential.

Substituting eqs. (6) and (10) into equation (13) and using equation (14), yields

$$\underline{\underline{\rho}}^{-1}\frac{\partial v_s}{\partial n} + \underline{\underline{\rho_s}}^{-1}\frac{\partial v_p}{\partial n} = -\frac{r\cos(r,n)}{B}v_s + r\cos(r,n)v_p\left(\frac{1}{B_p}-\frac{1}{B}\right) \qquad \text{on} \quad \Gamma_\infty. \tag{15}$$

3 FE APPROXIMATION

The application of the finite element (FE) method to the 3D resistivity problem for isotropic structures was dicussed by Pridmore et al (1981), Zhou & Greenhalgh (2001), and Li & Spitzer (2001). Here we solve the 3D problem for anisotropic structures using the FE technique. At first, we derive the variational integral using the variational principle. Following the formulation of Li & Spitzer (2001), the variational functional corresponding to eq. (9) is

$$I(v_s) = \int_\Omega \left[\underline{\underline{\rho}}^{-1}(\nabla v_s)^2 + 2\underline{\underline{\rho_s}}^{-1}\nabla v_p\cdot\nabla v_s\right] d\Omega, \tag{16}$$

where Ω denotes the model volume.
Taking the variation of the right-hand side of eq. (16) with respect to v_s, gives

$$\delta I(v_s) = \int_\Omega 2\left(\underline{\underline{\rho}}^{-1}\nabla v_s + \underline{\underline{\rho_s}}^{-1}\nabla v_p\right)\cdot\nabla\delta v_s d\Omega. \tag{17}$$

After carrying out integration by parts and substituting for the boundary conditions eqs. (11), (15) and (17) becomes

$$\delta I(v_s) = -\delta\int_{\Gamma_\infty}\left(\frac{r\cos(r,n)}{B}v_s^2 + 2r\cos(r,n)\left(\frac{1}{B}-\frac{1}{B_p}\right)v_p v_s\right)d\Gamma. \tag{18}$$

Hence, the solution of the boundary value problem consisting of eqs. (9), (11) and (15) gives a stationary value to the following functional:

$$\begin{aligned} F(v_s) &= \int_\Omega \left[\underline{\underline{\rho}}^{-1}(\nabla v_s)^2 + 2\underline{\underline{\rho_s}}^{-1}\nabla v_p\cdot\nabla v_s\right] d\Omega \\ &+ \int_{\Gamma_\infty}\left(\frac{r\cos(r,n)}{B}v_s^2 + 2r\cos(r,n)\left(\frac{1}{B}-\frac{1}{B_p}\right)v_p v_s\right)d\Gamma. \end{aligned} \tag{19}$$

The model volume Ω is subdivided into hexahedral elements, and the integrals of eq. (19) thus decompose into integrals for each element, in which the resistivity tensor is constant. It reads

$$F(v_s) = \sum_{e=1}^{n_e}\int_{\Omega_e}\underline{\underline{\rho}}^{-1}(\nabla v_s)^2 + \sum_{\Gamma_\infty}\int_{\Gamma_e}\frac{r\cos(r,n)}{B}v_s^2 d\Gamma$$

$$+ \quad 2\left[\sum_{e=1}^{n_e}\int_{\Omega_e}\underline{\underline{\rho_s}}^{-1}\nabla v_p\cdot\nabla v_s d\Omega+\sum_{\Gamma_\infty}\int_{\Gamma_e} r\cos(r,n)\left(\frac{1}{B}-\frac{1}{B_p}\right)v_p v_s d\Gamma\right], \tag{20}$$

where Ω_e denotes the volume of a particular element e and Γ_e the surface element on Γ_∞. n_e is the number of the hexahedral elements. The primary and secondary potentials are approximated in each element by linear representations:

$$v_p=\sum_{i=1}^{8}N_i v_{p,i}, \qquad v_s=\sum_{i=1}^{8}N_i v_{s,i} \tag{21}$$

where N_i are linear shape functions (Li & Spitzer, 2001), while $v_{p,i}$ and $v_{s,i}$ are the primary potential and the secondary potential at the corner points $i, i=1,\cdots,8$. By Substituting the linear representations (21) into equation (20) and evaluating the volume integrals over Ω_e and the boundary integral on Γ_e, we obtain the element integral. Summing up the integrals over all the elements, assembling the element matrix to a system matrix, and setting the first variation of the functional $F(v_s)$ with respect to v_s to zero results in the finite element equation

$$\mathsf{K}\mathsf{V_s}=-\mathsf{P} \tag{22}$$

where the system matrix K is symmetric and sparsely occupied by non-zero elements, $\mathsf{V_s}$ is a vector consisting of the unknown values of the secondary potentials at all nodes, and P is the known vector respresenting the source distribution due to the anomalous resistivity structure.
This system of linear equations is solved numerically using a preconditioned conjugate gradient method. The incomplete Cholesky decompostion has been proved to be a fast and efficient preconditioner for 3D resistivity modelling (Zhou & Greenhalgh 2001; Li & Spitzer 2001).

4 NUMERICAL TESTS

To test the FE techniques described in the previous sections, a two-layer model with azimuthal anisotropy (Fig. 1) is simulated. The resistivities of the top layer of thickness 5 *m* are assumed to be $\rho_{x1}=\rho_{z1}=\rho_{l1}=100\ \Omega m$, $\rho_{y1}=\rho_{t1}=10\ \Omega m$ and those of the bottom layer to be $\rho_{x2}=\rho_{z2}=\rho_{l2}=10\ \Omega m$ and $\rho_{y2}=\rho_{t2}=1\ \Omega m$. The single current source is located at the origin. The FE grid consists of $79\times79\times46$ nodes. The boundaries are located at ±500 *m* in *x*- and *y*-direction and at 500 *m* in *z*-direction. Fig. 2 shows the apparent resistivities of a pole-pole sounding in *x*- and *y*-direction. The analytical solutions computed by an analytical method (Wait 1990) are also shown for comparison. From Fig. 2, one can see that:

1) the computed FE results agree well with the analytical solutions at all grid nodes, especially the algorithm provides very accurate results near the source and at boundaries, which is due to the incorporation of the singularity removal technique and mixed boundary conditions. The average errors, which are calculated as being the sum of the percent error at all profile nodes divided by the number of nodes, are 0.36 per cent and 0.23 per cent for the sounding in *x*- and *y*-direction, respectively.

2) For the sounding in *y*-direction, we obtain an apparent resistivity of approximately 100 Ωm at small electrode spacings (the real resistivity of the top layer in *x*-direction) and of 10 Ωm at the large electrode spacings (the real resistivity of the bottom layer in *x*-direction). This is known as the anisotropy paradox.

3) For the sounding in *x*-direction, we obtain an apparent resistivity of approximately 31.6 Ωm at small electrode spacings (the geometric mean of the ρ_{l1} and ρ_{t1}) and of 3.16 Ωm at large electrode spacings (the geometeric mean of the ρ_{l2} and ρ_{t2}).

5 EFFECTS OF ANISOTROPY

In this section, a simple anisotropic cube is used to demonstrate the effect of horizontal, vertical and dipping anisotropy on the geoelectric interpretation. The cube has a side length of 5 *m* and principal resistivities of $\rho_{x'}/\rho_{y'}/\rho_{z'}=100/5/100\ \Omega m$. It is embedded in an isotropic homogeneous half-space with a resistivity of 5 Ωm. For clarity, the computed contour maps of the apparent resistivity at the surface are shown for pole-pole configuration. The single current source is located at the origin. All the calculations are made on a grid of $81\times81\times47$.

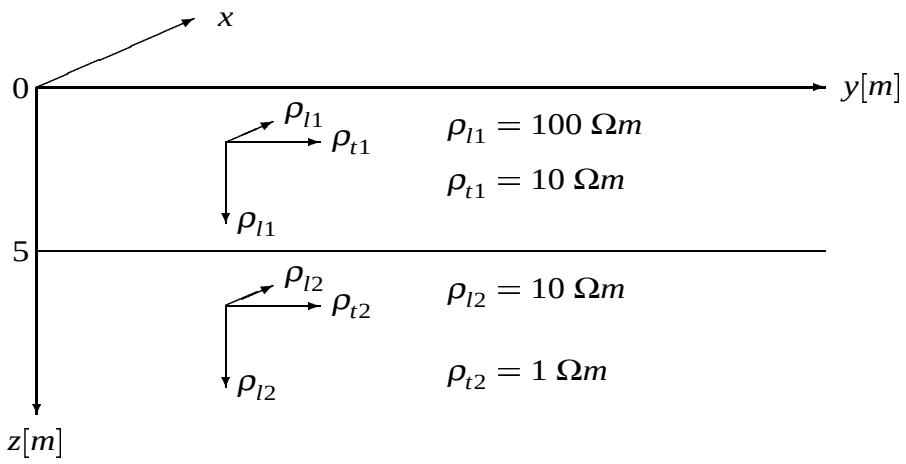

Fig. 1 A two-layer model with azimuthal anisotropy.

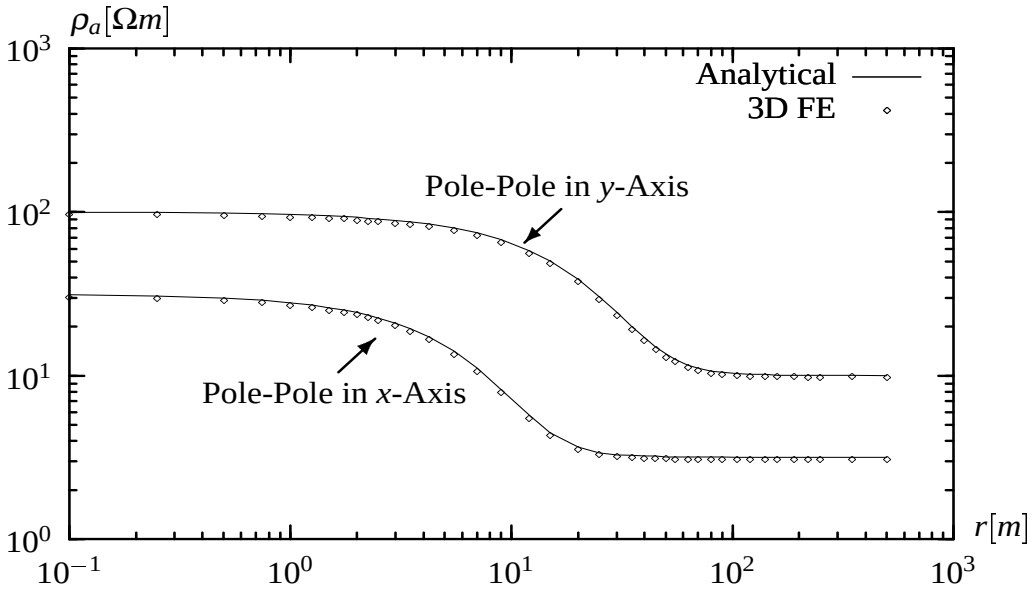

Fig. 2 Apparent resistivity of a pole-pole configuration for the model in Fig. 1 and different array orientations. Solid line - analytical solution; diamonds - results of the FE algorithm described in this paper.

5.1 Horizontal anisotropy

Fig. 3 shows the orientation of the principal axes. The principal axis z' is vertical, the remaining two principal axes x' and y' are in the horizontal plane (x,y) at an angle α with respect to the x axis. Fig. 4 shows the contour maps of the apparent resistivity for three different angles α $(0^0, 45^0, 90^0)$. For small distances between the current source and measuring points, the influence of the anisotropic cube can hardly be seen. With increasing distance the influence of the embedded anisotropic cube becomes more and more obvious, the isopleths are nearly ellipses. The maximum and minimum axes indicate the direction of the low and high resistivity, respectively, which is again due to the anisotropy paradox. Far from the inhomogeneity, the anomalous field fades out, the ρ_a approaches the resistivity of the isotropic half-space.

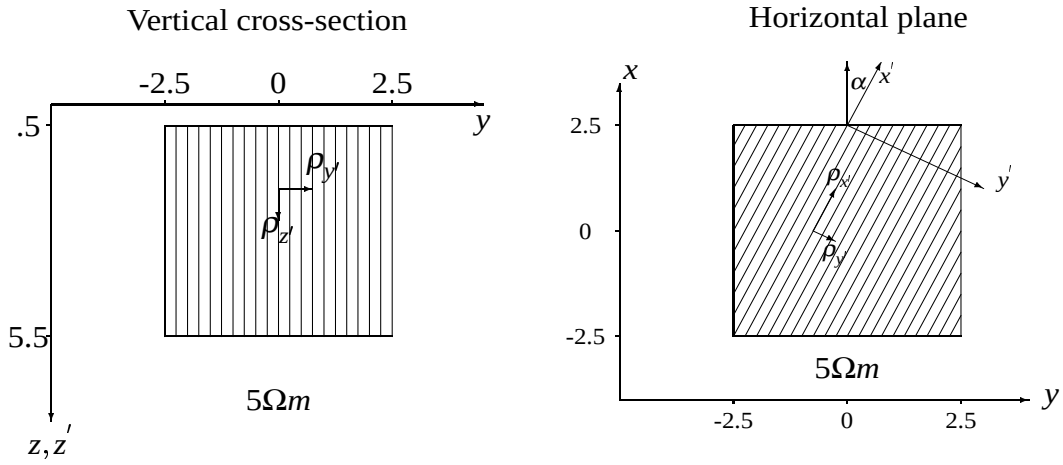

Fig. 3 A 3D cube with horizontal anisotropy in an isotropic half-space with $\rho = 5\ \Omega m$. The resistivity tensor of the cube is given by the principal resistivities $\rho_{x'}/\rho_{y'}/\rho_{z'} = 100/5/100\ \Omega m$ for varying angles α.

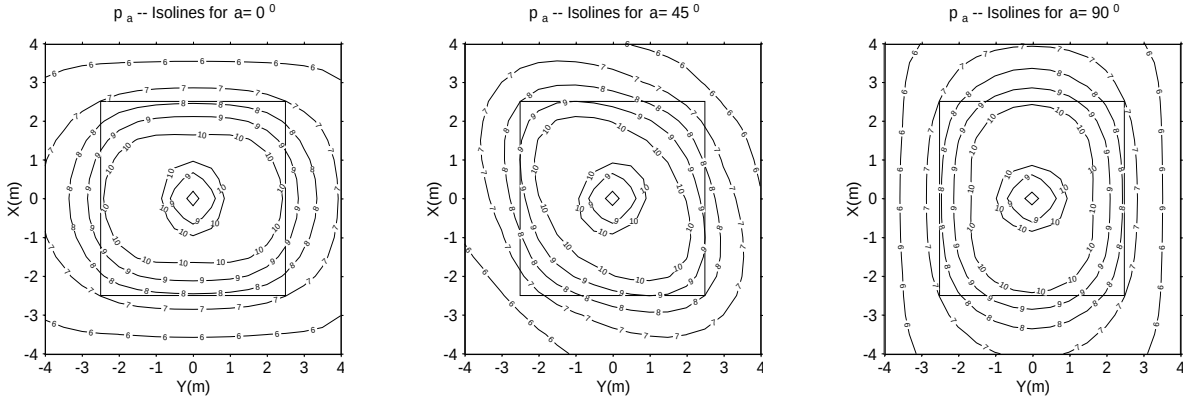

Fig. 4 A contour plot of the apparent resistivity for the pole-pole configuration of the Fig. 3 and various angles α.

5.2 Dipping anisotropy

Fig. 5 shows the orientation of the principal axes. The principal axis x' is horizontal and in the x-direction, the remaining two principal axes y' and z' are in the vertical plane (y,z) at a dip angle β with respect to the y axis. The top panel of Fig. 6 shows the contour maps of the apparent resistivity for three dip angles $\beta(=30^0, 45^0, 60^0)$. Again, for small distances the influence of the anisotropic cube can hardly be seen. For larger distances the isopleths are non-symmetric with respect to the x-axis ($y=0$) and are enlogated in the x- and y-directions at the right-hand side of each map. Note the existence of two asymmetric maxima left and right to the source point. Their magnitudes change with the dip angle β. It can more clearly be understood by looking at the apparent resistivity curves along the y-axis shown in the bottom panel of Fig. 6. We explain this behaviour by the distribution of the current density in the earth. In an anisotropic medium the current density is generally given by a linear combination of all three components of the electric field. From eqs. (3) and (4), the $y-$ and $z-$components of the current density in the $yz-$plane are expressed by

$$j_y(y,z) = -\sigma_{yy}\frac{\partial v}{\partial y} - \sigma_{yz}\frac{\partial v}{\partial z}, \tag{23}$$

$$j_z(y,z) = -\sigma_{yz}\frac{\partial v}{\partial y} - \sigma_{zz}\frac{\partial v}{\partial z}. \tag{24}$$

Fig. 7 shows the distribution of the current density in the $yz-$plane for three dipping angles $\beta(=30^0, 45^0, 60^0)$. The starting point of earch arrow is at the finite-element node. The length and the direction of the arrow

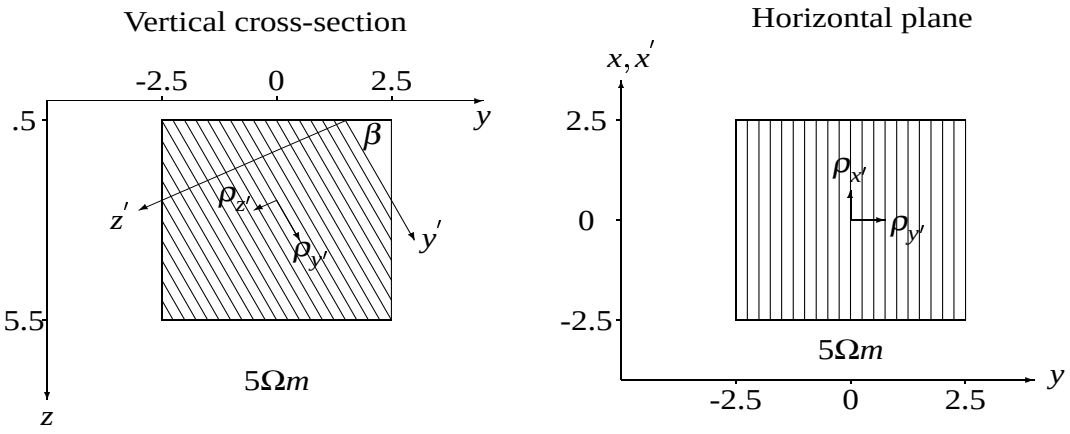

Fig. 5 A 3D cube with dipping anisotropy in an isotropic half-space with $\rho = 5\ \Omega m$. The resistivity tensor of the cube is given by the principal resistivities $\rho_{x'}/\rho_{y'}/\rho_{z'} = 100/5/100\ \Omega m$ for varying dip angles β.

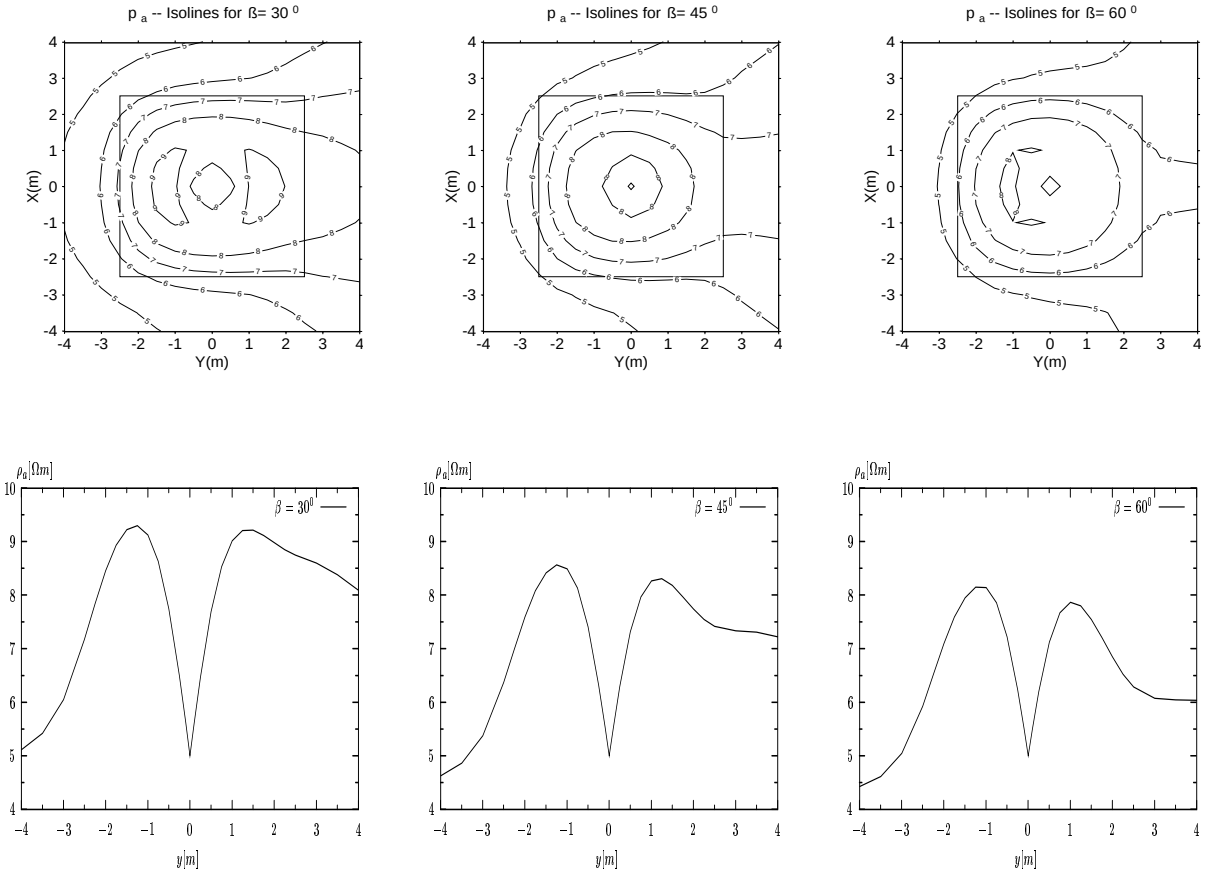

Fig. 6 A contour plot of the apparent resistivity (top) and sounding curves along the *y*-axis (bottom) for the pole-pole configuration of the Fig. 5 and various dip angles β.

reflect the magnitude and direction of the current density at that point. One can clearly see that the magnitude and direction of the current density change with the dipping angle β within the anisotropic cube, and the current flows mainly in the direction of the low resistivity.

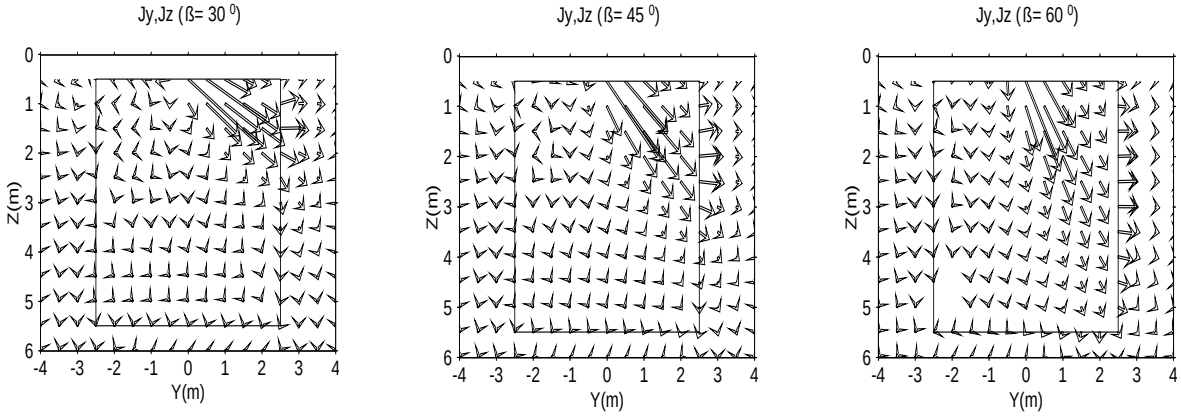

Fig. 7 The distribution of the current density in the *yz*-plane for the model in Fig. 5.

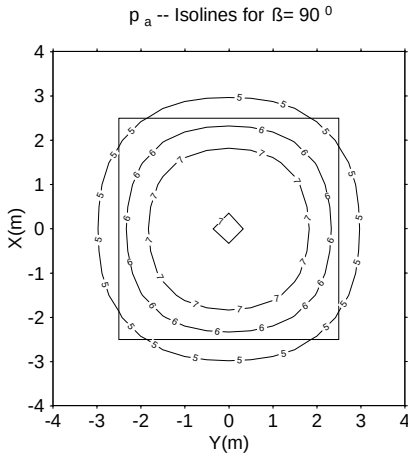

Fig. 8 A contour map of the apparent resistivity for the pole-pole configuration and a vertically anisotropic case.

5.3 Vertical anisotropy

The principal axes x', y' and z' are coincident with the *x*,*y* and *z*-axes, respectively, and the resistivity is axially symmetric with respect to *z*, in which the resistivity for any horizontal direction differs solely from that in vertical direction. Fig. 8 shows the contour map of the apparent resistivity, which is identical with the dipping anisotropy for $\beta = 90^0$. The isopleths are nearly circles centred at the origin. This means that the vertical anisotropy cannot be seen from geoelectrical data.

6 CONCLUSIONS

In this paper we have presented a newly developed finite-element algorithm for numerical modeling of geoelectrical fields in anisotropic 3D structures. The algorithm allows the simulation of arbitrary anisotropies in three dimensions, including the special cases of the horizontal, vertical and dipping anisotropy. The singularity removal procedure and mixed boundary conditions are incorporated, yielding a high degree of accuracy. The 3D simulation results show that the anisotropy has rendered the geoelectrical field more complex.

7 ACKNOWLEDGMENTS

This work is supported by the Deutsche Forschungsgemeinschaft (Ja 590/18-1).

REFERENCES

Bhattacharya, P.K. & Patra, H.P., 1968. *Direct current geoelectric sounding*, Elsevier publishing company.

Busby, 2000. The effectiveness of azimuthal apparent resistivity measurements as a method for determining fracture strike orientations, *Geophysical prospecting*, **48**, 677-695.

Habberjam, G.M., 1979. *Apparent resistivity observations and the use of square array techniques*, Geoexploration Monographs No. 9., Berlin.

Leonard-Mayer, P.J., 1984. A surface resistivity method for measuring hydrologic characteristics of jointed formations, *Report of investigations 8901, Bureau of mines, United States Department of the Interior*.

Li, P. & Uren, N.F., 1997. Analytical solution for the point source potential in an anisotropic 3-D half-space I: two-horizontal-layer case, *Mathem. Comp. Modelling*, **26**, 9-27.

Li, Y. & Spitzer, K. 2001. Three-dimensional DC resistivity finite element and finite difference forward modeling in comparison, submitted to *Geophysical Journal International*.

Lowry, T., Allen, M.B. & Shive, P.N., 1989. Singularity removal: a refinement of resistivity modeling techniques, *Geophysics*, **54**, 766-774.

Matias, M.J.S., 2002. Square array anisotropy measurements and resistivity sounding interpretation, *Journal of Applied Geophysics*, (in press).

Pridmore, D., Hohmann, G.W., Ward, S.H. & Sill, W.R., 1981. An investigation of finite element modeling for electrical and electromagnetic modeling data in three dimensions, *Geophysics*, **46**, 1009-1024.

Taylor, R.W. & Fleming, A.H., 1988. Characterizing jointed systems by azimuthal resistivity surveys, *Ground water*, **26**, 464-474.

Verner, T. & Pek, J., 1998. Numerical modelling of direct currents in 2-D anisotropic structures, in Protokoll Kolloquium *Elektromagnetische Tiefenforschung*, Neustadt an der Weinsrtraße 9.-13. 3. 1998, eds. Bahr,K. & Junge,A., DGG, 228-237.

Wait, J.R., 1990. Current flow into a 3-dimensionally anisotropic conductor, *Radio science*, **25**,689-694.

Watson, K.A. & Barker, R.D., 1999. Differentiating anisotropy and lateral effects using azimuthal resistivitiy offset Wenner soundings, *Geophysics*, **64**, 739-745.

Yin, Ch. & Weidelt, P., 1999. Geoelectrical fields in a layered earth with arbitrary anisotropy, *Geophysics*, **64**, 426-434.

Zhao, S. & Yedlin, M., 1996. Some refinements on the finite-difference method for 3-D dc resistivity modeling, *Geophysics*, **61**, 1301-1307.

Zhou, B. & Greenhalgh, S.A., 2001. Finite element three-dimensional direct current resistivity modeling: accuracy and efficiency considerations, *Geophys. J. Int.*, **145**, 679-688.